Available online at www.sciencedirect.com
ScienceDirect
Comput. Methods Appl. Mech. Engrg. 322 (2017) 541–562
Computer methods in applied mechanics and engineering
www.elsevier.com/locate/cma

Material point method with enriched shape function for crack problems ☆

Yong Liang, Tamas Benedek, Xiong Zhang*, Yan Liu

School of Aerospace Engineering, Tsinghua University, Beijing 100084, PR China

Received 22 November 2016; received in revised form 6 May 2017; accepted 9 May 2017
Available online 15 May 2017

Highlights

- The EMPM/EGIMP model cracks by enriching the nodal degrees of freedom as XFEM.
- The EMPM/EGIMP can degenerate to the conventional MPM/GIMP if there is no crack.
- Level Set Method is employed in the EMPM/EGIMP for easily tracking crack surfaces.

Abstract

A material point method (MPM)/generalized interpolation material point method (GIMP) with enriched shape function (EMPM/EGIMP for short) is proposed for modelling crack problems in the MPM/GIMP framework. The EMPM/EGIMP enriches the nodal degrees of freedom based on the idea of the extended finite element method (XFEM). This improvement allows the crack problem, whose displacement and velocity are discontinuous, to be simulated by only one set of background grid meshes, so multigrid and multiple velocity fields are unnecessary. In addition, the technique we developed to lump the mass matrix makes the EMPM/EGIMP can be implemented easily in a conventional MPM/GIMP code. If there is no crack, the EMPM/EGIMP degenerates to the conventional MPM/GIMP. The Level Set Method (LSM) is employed in the EMPM/EGIMP for easily tracking crack surfaces. The crack moves with the material points physically, so that the LSM function is carried by particles. In each time step, the LSM function value is mapped to the grid nodes from the particles, and the nodes to be enriched can be identified conveniently from the grid nodal LSM function values. Numerical experiments for stress fields distribution, fracture parameters calculation and crack propagation are provided to validate the proposed EMPM/EGIMP.

Keywords: Material point method; Crack propagation; Level set method; J integral; Stress intensity factor

☆ Supported by the National Natural Science Foundation of China) (11672154) and Science Challenge Project (JCKY2016212A502).
* Corresponding author.
E-mail address: xzhang@tsinghua.edu.cn (X. Zhang).

http://dx.doi.org/10.1016/j.cma.2017.05.012
0045-7825/

1. Introduction

In recent decades, fracture failure has resulted in a great loss in many fields, thus attracts researchers' attention. However, due to the huge complexity, not only the theoretical analysis is difficult to progress, even many experimental methods face lots of difficulties. With the rapid development of computer, numerical methods make a great progress in recent years, which provide a promising way to simulate dynamic fracture. Compared with the experimental methods, numerical methods have lower cost and can predict whole process of dynamic fracture.

Chen and Wilkins used the finite difference method (FDM) [1] to solve fracture mechanics problems. Later, the finite element method (FEM) is also capable of solving such problems. Based on the FEM, many methods have been developed for crack problems, such as the conventional FEM with adaptive mesh [2], cohesive zone model [3], node force release method, and embedded discontinuous method [4]. These methods can handle cracks by embedding them in the mesh, but have difficulties in dealing with crack propagation. Because the conventional FEM cannot describe discontinuous surfaces within elements, cracks have to propagate along the element boundaries or given paths, which limit the crack propagation in arbitrary directions. Therefore, updating the mesh to match the geometry of the discontinuity is necessary to simulate crack propagation, and it takes much higher computational cost and might cause a great decrease in calculation accuracy due to information mapping.

To ease the above difficulties in modelling crack propagation, the extended finite element method (XFEM) [5] was proposed, which introduces discontinuity within elements. The XFEM allows the arbitrary curved cracks to be handled independently of the mesh, so that remeshing is not necessary to model crack propagation. Later, Daux et al. [6] simulated arbitrary branched and intersecting cracks in the XFEM framework by superposing several Heaviside enrichment functions at the junctions. Budyn et al. [7] modelled the growth of multiple cracks. Sukumar et al. [8] developed XFEM for simulation of three-dimensional crack problems. Recently, the XFEM has been enhanced to simulate many challenges in computational fracture mechanics and composite modelling such as fracture in shell structures [9], band structure of metamaterials with microstructures [10], hydraulic fracture propagation [11,12], etc. However, the XFEM is developed on the basis of the FEM, so it still suffers the mesh distortion difficulty in large deformation problems.

Meshless method [13] constructs approximate functions without using a grid, so it does not suffer mesh distortion difficulty in some challenging problems such as impact, penetration, and explosion. Many meshless methods have been developed for dynamic fracture analysis [14] such as the element free Galerkin [15] (EFG) method, meshless local Petrov–Galerkin [16] (MLPG) method, just to name a few. The crack can easily propagate in arbitrary directions in meshless methods which is superior to the FEM. The difficulty in these meshless methods is the definition of particle "influence" zones around the crack, which should be able to describe the crack and handle crack surface contact.

The Material point method (MPM) is an extension of the particle-in-cell (PIC) method developed by Sulsky et al. [17,18]. In the MPM framework, a material domain is discretized into a set of particles moving through a predefined Eulerian background grid. The grid is used as a computational scratch pad to solve the equations of momentum, and then the grid solution is mapped back to the particles to update their physical quantities. At the end of every time step, the deformed grid is discarded, so that the mesh distortion is avoided for problems with large deformation [17]. Later, the generalized interpolation material point (GIMP) method was proposed by Bardenhagen et al. [19] using a Petrov–Galerkin formulation to alleviate the cell crossing noise. Throughout the last 20 years, the MPM was continuously developed and applied successfully to many challenging problems such as hyper velocity impact [20–23], explosion [24–26], penetration [27–29], fragmentation [30,31], and multiphase flow [32].

The advantages make the MPM preliminarily be applied to the simulation of fracture mechanics. The implementation of cracks within the framework of the MPM mainly includes two kinds of simulation methods. In the first kind, the multiple velocity fields are applied to describe the crack. Nairn proposed a method named CRAMP [33] (MPM with cracks) which simulates a crack by three types of velocity fields: one for particles on the same side of the crack relative to the node, one for particles above the crack relative to the node, and one for particles below the crack relative to the node. Although three velocity fields are defined, each node will have at most two velocity fields. Wang et al. [34] simulated two-dimensional mixed mode crack using an irregular mesh and the surfaces of the crack are introduced by allowing the placement of two sets of nodes along the crack line. Daphalapurkar et al. [35] simulated the dynamic crack growth by implementing a cohesive zone model in the generalized interpolation material point (GIMP) method. On the contrary, the second class of methods does not introduce the explicit crack, but uses a collection of failure particles to determine the approximate position of the crack. Chen et al. [36] simulated many fracture problems by this method and developed a failure criterion based on a bifurcation analysis. Yang et al. [30] simulated fragmentation

based on the Gurson model and random failure. Yang et al. [37] also simulated crack evolution by an improved decohesion model. This kind of method usually has difficulties in calculating the fracture parameters since the crack surface is not explicit, which is of significance to the crack propagation.

In this paper, we propose a material point method/generalized interpolation material point method with enriched shape function (EMPM/EGIMP for short), which is capable of modelling crack problems. The EMPM/EGIMP introduces the basic ideas of the XFEM into the MPM/GIMP, allowing local enrichment functions to be easily incorporated into the MPM/GIMP background grid. Therefore, multiple velocity fields and multiple background meshes are unnecessary. The quantities of particle (such as displacement, velocity) can be approximated by the standard finite element approximation and the discontinuous enrichment. For the simulation of the crack, only the nodes in the region around the crack are enriched by additional degrees of freedom and a discontinuous function is chosen as the enrichment function to model the jump in displacement across the crack line. To improve the efficiency, a mass lumping technique is also proposed which makes the EMPM/EGIMP be implemented easily in a conventional MPM/GIMP code, such as MPM3D [28], so that the EMPM/EGIMP costs only a little extra computation effort compared to the original MPM/GIMP. For tracking the crack line (surface in 3D), the EMPM/EGIMP employs the level set method (LSM). The level set function values, containing the information of the crack surface, are carried by the particles just as the other physical quantities, which is compatible with the MPM/GIMP framework. The proposed EMPM/EGIMP shows good performance in all the numerical experiments including stress fields distribution, fracture parameters calculation and crack propagation.

The paper is organized as follows. Section 2 briefly reviews the governing equations and the conventional MPM/GIMP scheme. The detailed formulation of the proposed EMPM/EGIMP is presented in Section 3, which also describes the LSM used to track the crack line, time integration and update of particle characteristic variables. Section 4 presents the algorithm for computing fracture parameters and introduces the dynamic crack propagation law, while Section 5 gives several numerical examples to validate the proposed method. Finally, Section 6 draws a summary and some concluding remarks.

2. Material point method

2.1. Governing equations

Consider the material domain Ω subjected to traction and displacement boundary conditions. The governing equations in updated Lagrange frame are given by

$$\rho\left(\boldsymbol{X},t\right)J\left(\boldsymbol{X},t\right)=\rho_0\left(\boldsymbol{X}\right)\quad\text{in}\quad\Omega \tag{1}$$

$$\sigma_{ij,j}+\rho b_i-\rho\ddot{u}_i=0\quad\text{in}\quad\Omega \tag{2}$$

with boundary conditions

$$\sigma_{ij}n_j=\bar{t}_i\quad\text{on}\quad\Gamma_t \tag{3}$$

$$u_i=\bar{u}_i\quad\text{on}\quad\Gamma_u \tag{4}$$

where ρ is the current density, $\boldsymbol{X}$ is the Lagrange coordinate, t is the current time, J is the Jacobian determinant, σ_{ij} is the Cauchy stress, b_i is the body force per unit mass, $\ddot{u}_i$ is the acceleration and subscripts i and j indicate the components of the spatial variables following Einstein convention, n_j is the unit outward normal, u_i is the displacement, Γ_t and Γ_u are the prescribed traction boundary and displacement boundary of Ω, respectively.

Taking the virtual displacement $\delta u_i(\delta u_i|_{\Gamma_u}=0)$ as the test functions, the weak form of the momentum Eq. (2) and traction boundary Eq. (3) can be obtained as

$$\int_\Omega\rho\ddot{u}_i\delta u_i\mathrm{d}\Omega+\int_\Omega\sigma_{ij}\delta u_{i,j}\mathrm{d}\Omega-\int_\Omega\rho b_i\delta u_i\mathrm{d}\Omega-\int_{\Gamma_t}\bar{t}_i\delta u_i\mathrm{d}\Gamma=0. \tag{5}$$

2.2. MPM solution scheme

In the MPM, the material domain Ω is discretized into a collection of particles, and the background grid serves as a computational scratch pad to solve the equation of momentum. At every time step the particles are attached to the

background grid. Therefore, the particle displacement u_{ip} can be obtained by interpolating the grid nodal displacement u_{iI} as

$$u_{ip} = N_{Ip} u_{iI} \tag{6}$$

where the subscript p denotes the variables associated with the particle p, the subscript I denotes the variables associated with the grid node I following Einstein convention, and N_{Ip} is the shape function of node I evaluated at the position of particle p.

Taking the particles as the quadrature points in the weak form Eq. (5) and applying the arbitrariness of the virtual displacement δu_{iI} lead to

$$\dot{p}_{iI} = m_I \ddot{u}_{iI} = f_{iI}^{\text{int}} + f_{iI}^{\text{ext}} \tag{7}$$

where

$$p_{iI} = m_I v_{iI} \tag{8}$$

is the grid nodal momentum,

$$m_I = \sum_{p=1}^{n_p} N_{Ip} m_p \tag{9}$$

is the lumped grid nodal mass by row summation,

$$f_{iI}^{\text{int}} = -\sum_{p=1}^{n_p} \frac{m_p}{\rho_p} N_{Ip,j} \sigma_{ijp} \tag{10}$$

is the internal nodal force, and

$$f_{iI}^{\text{ext}} = \sum_{p=1}^{n_p} m_p N_{Ip} b_{ip} \tag{11}$$

is the external nodal force. The traction term is omitted in Eq. (11) for simplicity.

2.3. GIMP

The MPM would produce noise in the numerical solution while material points cross background grid boundaries, called cell crossing noise [17]. To alleviate the cell crossing noise, Bardenhagen [19] first proposed the GIMP, which uses a Petrov–Galerkin discretization scheme and discretizes the material domain as a collection of particles defined by a characteristic function χ_p. The characteristic function defines the spatial volume occupied by the particle and should be a partition of unity in the initial configuration. Then, any material property (density, velocity, acceleration, etc.) can be approximated as

$$f(\boldsymbol{x}) = \sum_{p=1}^{n_p} f_p \chi_p(\boldsymbol{x}). \tag{12}$$

The test function is chosen as

$$\delta u_i = N_I \delta u_{iI}. \tag{13}$$

Substituting Eqs. (12) and (13) into the weak form Eq. (5) and applying the arbitrariness of the virtual displacement δu_{iI}, the grid nodal momentum equations of the GIMP can be obtained as

$$\dot{p}_{iI} = f_{iI}^{\text{int}} + f_{iI}^{\text{ext}} \tag{14}$$

where

$$p_{iI} = \sum_{p=1}^{n_p} S_{Ip} p_{ip} \tag{15}$$

$$f_{iI}^{\text{int}} = -\sum_{p=1}^{n_p} \sigma_{ijp} S_{Ip,j} V_p \tag{16}$$

$$f_{iI}^{\text{ext}} = \sum_{p=1}^{n_p} m_p S_{Ip} b_{ip}. \tag{17}$$

V_p is the particle volume defined by the spatial integral of χ_p, and

$$S_{Ip} = \frac{1}{V_p} \int_{\Omega_p \cap \Omega} \chi_p(\boldsymbol{x})\, N_I(\boldsymbol{x})\, d\Omega \tag{18}$$

is the GIMP shape function. When the characteristic function is chosen as

$$\chi_p(\boldsymbol{x}) = \delta\left(\boldsymbol{x} - \boldsymbol{x}_p\right) V_p \tag{19}$$

where $\boldsymbol{x}_p$ is the particle position, then the GIMP degenerates into the MPM.

The simplest characteristic function in 1D cases is

$$\chi_p(\boldsymbol{x}) = \begin{cases} 1, & \boldsymbol{x} \in \Omega_p \\ 0, & \text{otherwise} \end{cases} \tag{20}$$

where Ω_p depends on the particle domain. This particle characteristic function defines "contiguous particles", so the corresponding GIMP was denoted as the contiguous particle GIMP (cpGIMP) [38]. The grid shape function N_I is usually selected (for one dimension) as

$$N_I(x) = \begin{cases} 0, & |x - x_I| \geqslant L \\ 1 + (x - x_I)/L, & -L < x - x_I \leqslant 0 \\ 1 - (x - x_I)/L, & 0 < x - x_I < L \end{cases} \tag{21}$$

where x_I is the node position and L is the cell length. Substituting Eqs. (20) and (21) into Eq. (18) results in the GIMP shape function with C^1 continuity (for one dimension) as follows:

$$S_{Ip} = \begin{cases} 0, & |x_p - x_I| \geqslant L + l_p \\ \dfrac{\left(L + l_p + \left(x_p - x_I\right)\right)^2}{4Ll_p}, & -L - l_p < x_p - x_I \leqslant -L + l_p \\ 1 + \dfrac{x_p - x_I}{L}, & -L + l_p < x_p - x_I \leqslant -l_p \\ 1 - \dfrac{\left(x_p - x_I\right)^2 + l_p^2}{2Ll_p}, & -l_p < x_p - x_I \leqslant l_p \\ 1 - \dfrac{x_p - x_I}{L}, & l_p < x_p - x_I \leqslant L - l_p \\ \dfrac{\left(L + l_p - \left(x_p - x_I\right)\right)^2}{4Ll_p}, & L - l_p < x_p - x_I \leqslant L + l_p, \end{cases} \tag{22}$$

where l_p is half-length of the particle. In this paper, uGIMP [38] is used, in which the particle size is kept fixed. If there are two particles in one cell (for one-dimension), we have $l_p = L/4$, and S_{Ip} is simplified as

$$S_{Ip}(\xi) = \begin{cases} \dfrac{7 - 16\xi^2}{8}, & \xi \leqslant 0.25 \\ 1 - \xi, & 0.25 < \xi \leqslant 0.75 \\ \dfrac{(5 - 4\xi)^2}{16}, & 0.75 < \xi \leqslant 1.25 \\ 0, & \xi > 1.25 \end{cases} \tag{23}$$

where $\xi = \left|\left(x_p - x_I\right)/L\right|$. For three-dimensional problems, the shape function is given as

$$S_{Ip}(\boldsymbol{x}) = S_{Ip}(\xi)\, S_{Ip}(\eta)\, S_{Ip}(\zeta) \tag{24}$$

where $\eta = \left|\left(y_p - y_I\right)/L\right|$, $\zeta = \left|\left(z_p - z_I\right)/L\right|$.

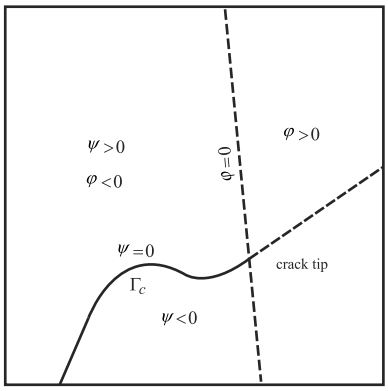

Fig. 1. Level set surfaces defining the crack line and the tips.

3. Material point method with enriched functions

3.1. Crack surface tracking by level set method

We employ the level set method [39] to describe the crack, which is one of the numerical methods tracking the discontinuous surface (such as crack, and boundary). In this section, the level set functions for the description of the crack are introduced. The crack with the crack tip is described by two level set functions. One describes the crack line (surface in 3D) and the other is used to find the crack tip. Therefore, we define the level set function ψ as the signed normal distance from particle p to the crack line ($\psi = 0$ defines the crack surface) and φ as the signed normal distance from particle p to the line which is perpendicular to the crack line and goes through the crack tip (the crack tip is on the line, $\varphi = 0$). Then the intersection is the crack tip as shown in Fig. 1.

At the end of every time step, the deformed grid is discarded, so the crack information should be carried by particles. The particles level set values are calculated in the initial configuration and remain unchanged as the analysis proceeds unless the crack propagates. The algorithm for calculating the level set values was presented in detail by Belytschko et al. [39]. At the beginning of every time step, the grid nodal level set values are extrapolated from particle level set values as

$$\psi_I = \frac{\sum_{p=1}^{n_p} N_{Ip} V_p \psi_p}{\sum_{p=1}^{n_p} N_{Ip} V_p} \qquad \varphi_I = \frac{\sum_{p=1}^{n_p} N_{Ip} V_p \varphi_p}{\sum_{p=1}^{n_p} N_{Ip} V_p} \tag{25}$$

where $\psi_I = \psi(\boldsymbol{x_I})$, $\psi_p = \psi(\boldsymbol{x_p})$, $\varphi_I = \varphi(\boldsymbol{x_I})$, $\varphi_p = \varphi(\boldsymbol{x_p})$, V_p is the particle volume and n_p is the number of the particles located in the cells containing the grid node I. The crack tip cells and cracked through cells can be identified by

$$\psi_{\text{cell}}^{\max} \psi_{\text{cell}}^{\min} < 0 \text{ and } \varphi_{\text{cell}}^{\max} \varphi_{\text{cell}}^{\min} < 0 \rightarrow \text{crack tip cell} \tag{26}$$

$$\psi_{\text{cell}}^{\max} \psi_{\text{cell}}^{\min} < 0 \text{ and } \varphi_{\text{cell}}^{\max} \varphi_{\text{cell}}^{\min} > 0 \rightarrow \text{crack through cell.} \tag{27}$$

3.2. Discontinuous enrichment

The displacement and velocity fields are continuous in the conventional MPM. In order to model cracks across which the displacement and velocity are discontinuous, the displacement of particle p can be approximated as

$$u_{ip} = \sum_{I=1}^{n_n} N_{Ip} u_{iI} + \sum_{R=1}^{n_c} H_{Rp} N_{Rp} q_{iR} \tag{28}$$

where the first term in the right hand side of Eq. (28) is the standard finite element approximation and the second term is the discontinuous enrichment. In the above, u_{iI} is the standard nodal degrees of freedom, q_{iR} is the enriched nodal degrees of freedom, n_n is the number of all grid nodes, n_c is the number of enriched grid nodes and H_{Rp} represents

the relationship between the node R and the particle p. If they are located in the same side of the crack then $H_{Rp} = 1$, otherwise $H_{Rp} = -1$. Namely

$$H_{Rp} = H(\psi_R, \psi_p) = \begin{cases} 1 & \text{if } \operatorname{sign}(\psi_R) = \operatorname{sign}(\psi_p) \\ -1 & \text{if } \operatorname{sign}(\psi_R) \neq \operatorname{sign}(\psi_p). \end{cases} \tag{29}$$

Note that only the nodes whose supports are cut by a crack are required to be enriched, so the EMPM costs only a little extra computation effort compared to the original MPM.

3.3. EMPM formulation

Substituting Eq. (28) into the weak form Eq. (5) leads to the discrete formulation of the proposed EMPM as

$$\begin{aligned} &\sum_{p=1}^{n_p} m_p \left[\sum_{I=1}^{n_n} N_{Ip} \delta u_{iI} + \sum_{R=1}^{n_c} H_{Rp} N_{Rp} \delta q_{iR} \right] \left[\sum_{J=1}^{n_n} N_{Jp} \ddot{u}_{iJ} + \sum_{L=1}^{n_c} H_{Lp} N_{Lp} \ddot{q}_{iL} \right] \\ &\quad + \sum_{p=1}^{n_p} \frac{m_p}{\rho_p} \sigma_{ijp} \left[\sum_{I=1}^{n_n} N_{Ip,j} \delta u_{iI} + \sum_{R=1}^{n_c} H_{Rp} N_{Rp,j} \delta q_{iR} \right] \\ &= \sum_{p=1}^{n_p} m_p b_{ip} \left[\sum_{I=1}^{n_n} N_{Ip} \delta u_{iI} + \sum_{R=1}^{n_c} H_{Rp} N_{Rp} \delta q_{iR} \right]. \end{aligned} \tag{30}$$

Invoking the arbitrariness of δu_{iI} and δq_{iR}, Eq. (30) can be rewritten in matrix form as

$$\begin{bmatrix} [m_{IJ}] & [m_{IL}] \\ [m_{RJ}] & [m_{RL}] \end{bmatrix} \begin{Bmatrix} [\ddot{u}_{iJ}] \\ [\ddot{q}_{iL}] \end{Bmatrix} = \begin{Bmatrix} [f_{iI}] \\ [f^*_{iR}] \end{Bmatrix} \tag{31}$$

where

$$m_{IJ} = \sum_{p=1}^{n_p} m_p N_{Ip} N_{Jp} \qquad m_{IL} = \sum_{p=1}^{n_p} m_p N_{Ip} H_{Lp} N_{Lp} \tag{32}$$

$$m_{RJ} = \sum_{p=1}^{n_p} m_p H_{Rp} N_{Rp} N_{Jp} \qquad m_{RL} = \sum_{p=1}^{n_p} m_p H_{Rp} N_{Rp} H_{Lp} N_{Lp} \tag{33}$$

$$f_{iI} = -\sum_{p=1}^{n_p} \frac{m_p}{\rho_p} N_{Ip,j} \sigma_{ijp} + \sum_{p=1}^{n_p} m_p N_{Ip} b_{ip} \tag{34}$$

$$f^*_{iR} = -\sum_{p=1}^{n_p} \frac{m_p}{\rho_p} H_{Rp} N_{Rp,j} \sigma_{ijp} + \sum_{p=1}^{n_p} m_p H_{Rp} N_{Rp} b_{ip}. \tag{35}$$

The terms f_{iI} and f^*_{iR} are the ith component of the conventional nodal force vector of grid node I and the enriched nodal force vector of grid node R respectively, which include both internal and external forces. Note that Eq. (31) gives the consistent mass matrix. m_{IJ} and m_{RL} correspond to the conventional and enriched degrees of freedom respectively, while m_{IL} and m_{RJ} are the coupled terms. The consistent mass matrix leads to a significant increase of cost. To improve solution efficiency, the lumped form of mass matrix is used. However, the subscripts, I and J, correspond to all the nodes as in the conventional MPM, while R and L just represent the enriched nodes. Therefore, the coupled mass matrices m_{IL} and m_{RJ} in Eq. (31) are not the square matrices, which causes the difficulties in lumping the nodal mass by row summation. Therefore, we introduced the enriched nodal degrees of freedom for those unenriched nodes to expand the mass matrices to square matrices.

Note that the matrices $[m_{IJ}]$ and $[m_{RJ}]$ can be lumped by the method used in the conventional MPM, while $[m_{IL}]$ and $[m_{RL}]$ cannot. To lump $[m_{IL}]$ and $[m_{RL}]$, we need to use the characteristics of the function H. According to the definition, we have

$$H_{Ip} H_{Ip} = 1 \tag{36}$$

$$H_{Ip}H_{Lp} = H_{IL} \tag{37}$$

where H_{IL} is defined by the same way with H_{Ip}, namely

$$H_{IL} = H(\psi_I, \psi_L) = \begin{cases} 1 & \text{if sign}(\psi_I) = \text{sign}(\psi_L) \\ -1 & \text{if sign}(\psi_I) \neq \text{sign}(\psi_L). \end{cases} \tag{38}$$

Substituting Eqs. (36) and (37) into m_{IS} and m_{RS} leads to

$$m_{IL} = \sum_{p=1}^{n_p} m_p N_{Ip} \left(H_{Ip}H_{Ip}\right) H_{Lp}N_{Lp} = \sum_{p=1}^{n_p} m_p H_{Ip}N_{Ip}H_{IL}N_{Lp} \tag{39}$$

$$m_{RL} = \sum_{p=1}^{n_p} m_p N_{Rp} \left(H_{Rp}H_{Lp}\right) N_{Lp} = \sum_{p=1}^{n_p} m_p N_{Rp}H_{RL}N_{Lp} \tag{40}$$

where the indices I, J, R and L have the same range of values, then all the submatrices are the square matrices. Substituting (39) and (40) into Eq. (31) leads to

$$\begin{bmatrix} [m_{IJ}] & [m^*_{IL}] \\ [m^*_{IJ}] & [m_{IL}] \end{bmatrix} \begin{Bmatrix} [\ddot{u}_{iJ}] \\ [H_{IL}\ddot{q}_{iL}] \end{Bmatrix} = \begin{Bmatrix} [f_{iI}] \\ [f^*_{iI}] \end{Bmatrix}. \tag{41}$$

where

$$m_{IJ} = \sum_{p=1}^{n_p} m_p N_{Ip}N_{Jp} \qquad m^*_{IL} = \sum_{p=1}^{n_p} m_p H_{Ip}N_{Ip}N_{Lp} \tag{42}$$

$$m^*_{IJ} = \sum_{p=1}^{n_p} m_p H_{Ip}N_{Ip}N_{Jp} \qquad m_{IL} = \sum_{p=1}^{n_p} m_p N_{Ip}N_{Lp}. \tag{43}$$

Then we can lump the above matrices as

$$m_I = \sum_{J=1}^{n_n} m_{IJ} = \sum_{L=1}^{n_n} m_{IL} = \sum_{p=1}^{n_p} m_p N_{Ip} \tag{44}$$

$$m^*_I = \sum_{J=1}^{n_n} m^*_{IJ} = \sum_{L=1}^{n_n} m^*_{IL} = \sum_{p=1}^{n_p} m_p H_{Ip}N_{Ip}. \tag{45}$$

Therefore, Eq. (41) is simplified by invoking $H_{II} = 1$ as

$$\begin{Bmatrix} [\dot{p}_{iI}] \\ [\dot{p}^*_{iI}] \end{Bmatrix} = \begin{bmatrix} [m_I] & [m^*_I] \\ [m^*_I] & [m_I] \end{bmatrix} \begin{Bmatrix} [\ddot{u}_{iI}] \\ [\ddot{q}_{iI}] \end{Bmatrix} = \begin{Bmatrix} [f_{iI}] \\ [f^*_{iI}] \end{Bmatrix}. \tag{46}$$

This is the final formulation where the coupled terms are reserved, which is very different with the conventional MPM. However, to simulate the problem including cracks, Eq. (46) should be solved, where $\dot{p}_{iI} = m_I\ddot{u}_{iI} + m^*_I\ddot{q}_{iI}$ is no longer the rate of change of the regular nodal momentum. The aim we calculate $\ddot{u}_{iI}$ and $\ddot{q}_{iI}$ is to update the physical quantities of particles. Since we have introduced the enriched nodal degrees of freedom for those unenriched nodes in Eq. (28), the acceleration of particle p can be rewritten as

$$\ddot{u}_{ip} = \sum_{I=1}^{n_n} N_{Ip} \left(\ddot{u}_{iI} + H_{Ip}\ddot{q}_{iI}\right). \tag{47}$$

Therefore, we do not need to solve Eq. (46) directly, because we only need the combined term $\ddot{u}_{iI} + H_{Ip}\ddot{q}_{iI}$ to update the particle accelerations. Taking node I as an example, multiplying the second equation in Eq. (46) by H_{Ip} and then adding to the first equation result in

$$\dot{p}_{iI} + H_{Ip}\dot{p}^*_{iI} = \left(m_I + H_{Ip}m^*_I\right)\ddot{u}_{iI} + \left(m^*_I + H_{Ip}m_I\right)\ddot{q}_{iI} \tag{48}$$

where m_I and m^*_I are the two lumped masses for node I defined by Eqs. (44) and (45), and p represents the particle

we are updating. Invoking Eq. (36), Eq. (48) can be rewritten as

$$\ddot{u}_{iI} + H_{Ip}\ddot{q}_{iI} = \frac{\dot{p}_{iI} + H_{Ip}\dot{p}^*_{iI}}{m_I + H_{Ip}m^*_I}. \tag{49}$$

Substituting Eq. (49) into Eq. (47) gives

$$\ddot{u}_{ip} = \sum_{I=1}^{n_n} N_{Ip}\left(\frac{\dot{p}_{iI} + H_{Ip}\dot{p}^*_{iI}}{m_I + H_{Ip}m^*_I}\right). \tag{50}$$

Eq. (50) is what we used in this paper to update the particle quantities. For the nodes which are not enriched by the crack, the particles in its influence domain are always at the same side of the crack, which means H_{Ip}= 1 all the time. Then we find that $\dot{p}_{iI} = \dot{p}^*_{iI}$ and $m_I = m^*_I$, so Eq. (50) is degenerated to

$$\ddot{u}_{ip} = \sum_{I=1}^{n_n} N_{Ip}\frac{\dot{p}_{iI}}{m_I}. \tag{51}$$

Eq. (51) is the same with the equation in the conventional MPM and $\dot{p}_{iI}$ is the rate of change of the nodal momentum in ith direction. Therefore, the EMPM degenerates to the conventional MPM when there is no crack. That is to say, only the nodes in the region around the crack need to be enriched in computer implementation, although we introduced the enriched nodal degrees of freedom for those unenriched nodes to lump the mass matrix. Hence the EMPM costs only a little extra computation effort compared to the original MPM. Furthermore, we can observe that the expressions for node force and matrix in the EMPM are very similar to that in the conventional MPM, although the additional nodal degrees of freedom are introduced in the EMPM. Therefore, the EMPM is easy to be implemented in a conventional MPM code, such as the MPM3D code [28].

3.4. EGIMP formulation

The enriched shape function can also be incorporated in the GIMP to make it capable of modelling crack problems. The virtual displacement in the GIMP can be enriched similarly as

$$\delta u_i(\boldsymbol{x}) = \sum_{I=1}^{n_n} N_I(\boldsymbol{x})\,\delta u_{iI} + \sum_{R=1}^{n_c} H_R(\boldsymbol{x})\,N_R(\boldsymbol{x})\,\delta q_{iR} \tag{52}$$

where $\boldsymbol{x}$ is the spatial position and $H_R(\boldsymbol{x}) = H(\psi_R, \psi(\boldsymbol{x}))$ as defined in Eq. (29). In the GIMP, it is a reasonable assumption that the whole region Ω_p for particle p is at the same side of the crack, which results in $\text{sign}(\psi(\boldsymbol{x})) = \text{sign}(\psi_p)$ in the volume Ω_p. Thus

$$H_R(\boldsymbol{x}) = H(\psi_R, \psi(\boldsymbol{x})) = H\left(\psi_R, \psi_p\right) = H_{Rp}, \quad \boldsymbol{x} \in \Omega_p. \tag{53}$$

Substituting Eqs. (12) and (52) into the weak form Eq. (5) gives

$$\begin{aligned}
&\sum_{p=1}^{n_p}\int_{\Omega_p\cap\Omega}\frac{\dot{p}_{ip}}{V_p}\chi_p\left[\sum_{I=1}^{n_n} N_I(\boldsymbol{x})\,\delta u_{iI} + \sum_{R=1}^{n_c} H_{Rp}N_R(\boldsymbol{x})\,\delta q_{iR}\right]d\Omega \\
&\quad + \sum_{p=1}^{n_p}\int_{\Omega_p\cap\Omega}\sigma_{ijp}\chi_p\left[\sum_{I=1}^{n_n} N_{I,j}(\boldsymbol{x})\,\delta u_{iI} + \sum_{R=1}^{n_c} H_{Rp}N_{R,j}(\boldsymbol{x})\,\delta q_{iR}\right]d\Omega \\
&= \sum_{p=1}^{n_p}\int_{\Omega_p\cap\Omega}\rho_p b_{ip}\chi_p\left[\sum_{I=1}^{n_n} N_I(\boldsymbol{x})\,\delta u_{iI} + \sum_{R=1}^{n_c} H_{Rp}N_R(\boldsymbol{x})\,\delta q_{iR}\right]d\Omega.
\end{aligned} \tag{54}$$

Here we also introduced the enriched nodal degrees of freedom for those unenriched nodes similar to the EMPM. Invoking the arbitrariness of δu_{iI} and δq_{iR}, Eq. (54) can be rewritten in matrix form as

$$\begin{Bmatrix}[\dot{p}_{iI}]\\ [\dot{p}^*_{iR}]\end{Bmatrix} = \begin{Bmatrix}[f_{iI}]\\ [f^*_{iR}]\end{Bmatrix} \tag{55}$$

where

$$p_{iI} = \sum_{p=1}^{n_p} S_{Ip} p_{ip}, \qquad p^*_{iR} = \sum_{p=1}^{n_p} H_{Rp} S_{Rp} p_{ip} \tag{56}$$

$$f_{iI} = -\sum_{p=1}^{n_p} \sigma_{ijp} S_{Ip,j} V_p + \sum_{p=1}^{n_p} m_p S_{Ip} b_{ip}, \tag{57}$$

$$f^*_{iR} = -\sum_{p=1}^{n_p} \sigma_{ijp} H_{Rp} S_{Rp,j} V_p + \sum_{p=1}^{n_p} m_p H_{Rp} S_{Rp} b_{ip} \tag{58}$$

where S_{Ip} and S_{Rp} are the GIMP shape functions as defined in Eq. (18). Then the displacement of particle p can be approximated by the GIMP with enriched shape function as

$$u_{ip} = \sum_{I=1}^{n_n} S_{Ip} u_{iI} + \sum_{R=1}^{n_c} H_{Rp} S_{Rp} q_{iR}. \tag{59}$$

Substituting Eq. (59) into Eq. (55) gives

$$\begin{bmatrix} [m_{IJ}] & [m_{IL}] \\ [m_{RJ}] & [m_{RL}] \end{bmatrix} \begin{Bmatrix} [\ddot{u}_{iJ}] \\ [\ddot{q}_{iL}] \end{Bmatrix} = \begin{Bmatrix} [f_{iI}] \\ [f^*_{iR}] \end{Bmatrix} \tag{60}$$

where

$$m_{IJ} = \sum_{p=1}^{n_p} m_p S_{Ip} S_{Jp} \qquad m_{IL} = \sum_{p=1}^{n_p} m_p S_{Ip} H_{Lp} S_{Lp} \tag{61}$$

$$m_{RJ} = \sum_{p=1}^{n_p} m_p H_{Rp} S_{Rp} S_{Jp} \qquad m_{RL} = \sum_{p=1}^{n_p} m_p H_{Rp} S_{Rp} H_{Lp} S_{Lp}. \tag{62}$$

It should be noted that Eq. (60) is in the same form as Eq. (31) but replaces the MPM shape function with the GIMP shape function. Since the GIMP shape function is also a partition of unity, the mass matrix can be lumped in the same way as the EMPM and will not be repeated here.

3.5. Explicit time integration

Eq. (49) can be solved using the leapfrog explicit integration scheme as shown in Fig. 2 [17]. Hence, the two types of nodal momentum can be updated as

$$p^{n+1/2}_{iI} = p^{n-1/2}_{iI} + f^n_{iI} \Delta t^n \tag{63}$$

$$p^{*,n+1/2}_{iI} = p^{*,n-1/2}_{iI} + f^{*,n}_{iI} \Delta t^n \tag{64}$$

where the superscript n represents the time step. The particle position and velocity can be obtained by Eq. (50) as follows,

$$\begin{aligned} x^{n+1}_{ip} &= x^n_{ip} + \Delta t^{n+1/2} \sum_{I=1}^{n_n} N^n_{Ip} \frac{p^{n+1/2}_{iI} + H^n_{Ip} p^{*,n+1/2}_{iI}}{m^n_I + H^n_{Ip} m^{*,n}_I} \\ v^{n+1/2}_{ip} &= v^{n-1/2}_{ip} + \Delta t^n \sum_{I=1}^{n_n} N^n_{Ip} \frac{f^n_{iI} + H^n_{Ip} f^{*,n}_{iI}}{m^n_I + H^n_{Ip} m^{*,n}_I}. \end{aligned} \tag{65}$$

The shape function N^n_{Ip} should be replaced by S^n_{Ip} for the EGIMP.

4. Crack propagation modelling

4.1. J-integral and stress intensity factor calculation

The proposed EMPM/EGIMP method extends the ability of modelling cracks in the MPM/GIMP framework. To implement the crack propagation for simulating the whole process of fracture, the next mission is to calculate the

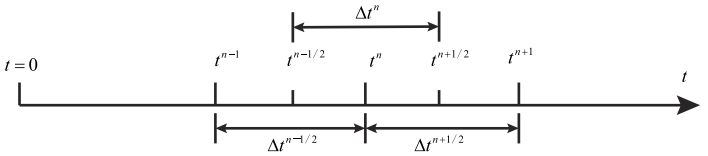

Fig. 2. Leapfrog time integrator scheme.

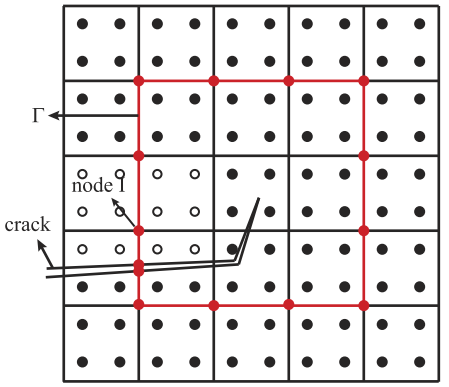

Fig. 3. The J- integral contour where red points are the integration points. (For interpretation of the references to colour in this figure legend, the reader is referred to the web version of this article.)

fracture parameters of the crack tip such as the energy release rate G and stress intensity factors K. This section introduces the calculation of J-integral around a crack tip, a key fracture parameter put forward by Cherepanov [40] and Rice [41] independently. Then we partition the J-integral into stress intensity factors K_1 and K_2, whose implementation has been described previously in CRAMP [42,43].

The key to the method is the calculation of the J-integral. Although the concept of J-integral was developed for quasi-static problems without considering the influence of the kinetic energy, it was later extended to dynamic problems by including kinetic energy. The definition of the dynamic J-integral components J_m ($m = 1, 2$) is given by [44,45]

$$J_m = \lim_{\varepsilon \to 0} \int_{\Gamma_\varepsilon} \left[(W + E)\, n_m - \sigma_{ij} n_j \frac{\partial u_i}{\partial x_m} \right] \mathrm{d}\Gamma \tag{66}$$

$$= \int_{\Gamma} \left[(W + E)\, n_m - \sigma_{ij} n_j \frac{\partial u_i}{\partial x_m} \right] \mathrm{d}\Gamma + \int_{\mathrm{A}(\Gamma)} \rho \left[\frac{\partial^2 u_i}{\partial t^2} \frac{\partial u_i}{\partial x_m} - \frac{\partial u_i}{\partial t} \frac{\partial^2 u_i}{\partial t \partial x_m} \right] \mathrm{dA} \tag{67}$$

where W is the stress work density, which is obtained by integrating $\mathrm{d}W = \sigma_{ij} \mathrm{d}\varepsilon_{ij}$, $E = \frac{1}{2} \rho \dot{u}_i \dot{u}_i$ is the kinetic energy density, σ_{ij} is the stress, ε_{ij} is the strain, n_m is the mth components of the unit normal to the integration contour (Γ or Γ_ε), $\partial u_i / \partial x_m$ is the displacement gradient, and $\partial u_i / \partial t$ is the velocity. The Γ is an arbitrary integration contour around the crack tip, while Γ_ε is the integration contour around the crack tip with the maximum radius ε. The $A(\Gamma)$ is the integration area enclosed by the contours Γ and Γ_ε. The result is path independent for static problem due to the area integral cancelled. For the dynamic problem, the property will be lost because the transmission of the energy to different paths depends on the time stress waves reach the path.

In this paper, Eq. (67) is computed by numerical integral over a path close to the crack tip, which has been proved to be precise enough previously [42]. With the path independence, a square curve on the background grid is chosen as shown in Fig. 3. The curve Γ is centred on the cell containing the crack tip and is denoted by an odd number n where n is the length of the square ($n = 3$ in Fig. 3).

We first identify the cell containing the crack tip, then the contour nodes can be easily identified. With the level set values the crossing point (where the crack surfaces cross the integration contour) can also be easily located. From the lower crack surface to the upper crack surface we set the integration points clockwise as shown in Fig. 3. Next

the integration data of these nodes are calculated by the local weighted least square method, which is different from the extrapolation. As shown in Fig. 3, the information of node I is calculated by the particles described by hollow circles whose weights are calculated from the shape function $N_I(\boldsymbol{x})$ in the conventional MPM. The distance between the particle and the node is less than one cell length in x or y direction and they are located on the same side of the crack. The method deals with the crossing point without extra effort. The integral is then evaluated using a simple midpoint numerical integration rule as

$$J_m = \sum_{k=1}^{n_J-1} \left(F_m^{(k)} + F_m^{(k+1)}\right) \frac{\Delta_k}{2} \qquad m = 1, 2 \tag{68}$$

$$F_m^{(k)} = \left(W^{(k)} + E^{(k)}\right) n_m^{(k)} - \sigma_{ij}^{(k)} n_j^{(k)} \frac{\partial u_i^{(k)}}{\partial x_m} \tag{69}$$

where subscript k denotes integration points and n_J denotes total number of integration points.

Once the J-integral is obtained, the dynamic energy release rate for elastic material, G, is given by [46]

$$G = J_1 \cos\theta + J_2 \sin\theta$$

where θ is the crack angle relative to the x-axis. Under the assumption of linear–elastic and homogeneous material, the relations between G and the stress intensity factors, K_{I} and K_{II}, are given [47] by

$$K_{\mathrm{I}} = \delta_{\mathrm{I}} \left\{ \frac{2\mu G \beta_2}{A_{\mathrm{I}} \left(\delta_{\mathrm{I}}^2 \beta_2 + \delta_{\mathrm{II}}^2 \beta_1\right)} \right\}^{1/2} \tag{70}$$

$$K_{\mathrm{II}} = \delta_{\mathrm{II}} \left\{ \frac{2\mu G \beta_1}{A_{\mathrm{II}} \left(\delta_{\mathrm{I}}^2 \beta_2 + \delta_{\mathrm{II}}^2 \beta_1\right)} \right\}^{1/2} \tag{71}$$

where μ is the shear modulus, δ_{I} and δ_{II} are the crack opening and shearing displacements respectively. The massless points are employed to track the crack opening displacements as CRAMP, which move with the background mesh just like the particle but have no influence to the grid node. The detailed expressions for the crack-velocity functions (β_1, β_2, A_{I}, A_{II}) are [48]

$$\beta_1 = \left(1 - C^2/C_{\mathrm{d}}^2\right)^{1/2} \tag{72}$$

$$\beta_2 = \left(1 - C^2/C_{\mathrm{s}}^2\right)^{1/2} \tag{73}$$

$$A_{\mathrm{I}} = \frac{\beta_1 \left(1 - \beta_2^2\right)}{4\beta_1\beta_2 - \left(1 + \beta_2^2\right)^2} \tag{74}$$

$$A_{\mathrm{II}} = \frac{\beta_2 \left(1 - \beta_2^2\right)}{4\beta_1\beta_2 - \left(1 + \beta_2^2\right)^2} \tag{75}$$

where C is the crack propagation velocity, C_{d} and C_{s} are the dilatational and shear-wave speeds, which depend on the material constants by

$$C_{\mathrm{d}}^2 = \frac{\kappa + 1}{\kappa - 1} \frac{\mu}{\rho}, \quad C_{\mathrm{s}}^2 = \frac{\mu}{\rho} \tag{76}$$

and

$$\kappa = \begin{cases} (3 - \nu) / (1 + \nu) & \text{(plane stress)} \\ 3 - 4\nu & \text{(plane strain)} \end{cases} \tag{77}$$

where ν is the Poisson's ratio. When the crack velocity is zero, Eqs. (70) and (71) are simplified [42] to

$$K_{\mathrm{I}} = \begin{cases} \dfrac{\delta_{\mathrm{I}}}{\delta} \sqrt{GE} & \text{(plane stress)} \\ \dfrac{\delta_{\mathrm{I}}}{\delta} \sqrt{\dfrac{GE}{1 - \nu^2}} & \text{(plane strain)} \end{cases} \tag{78}$$

$$K_{\mathrm{II}} = \begin{cases} \dfrac{\delta_{\mathrm{II}}}{\delta}\sqrt{GE} & \text{(plane stress)} \\ \dfrac{\delta_{\mathrm{II}}}{\delta}\sqrt{\dfrac{GE}{1-\nu^2}} & \text{(plane strain)} \end{cases} \tag{79}$$

where E is the tensile modulus.

4.2. Dynamic crack propagation law

In this paper, "the maximum stress criterion" is used as the fracture criterion, which was first studied by Erdogan and Sih [49] in 1963, both experimentally and analytically. The fracture criterion was stated as "the crack will start to grow from the tip in the direction along which the tangential stress σ_θ, is maximum and the shear stress $\tau_{r\theta}$, is zero". Based on this criterion, the maximum hoop stress angle θ_{c} can be obtained by maximizing the hoop stress near the crack tip as [50]

$$\theta_{\mathrm{c}} = 2\arctan\left[\frac{1}{4}\left(\frac{K_{\mathrm{I}}}{K_{\mathrm{II}}} - \mathrm{sign}(K_{\mathrm{II}})\left(8 + \left(\frac{K_{\mathrm{I}}}{K_{\mathrm{II}}}\right)\right)^{1/2}\right)\right]. \tag{80}$$

Then the corresponding maximum hoop stress intensity K^* can be calculated [51] by

$$K^* = \cos^3\left(\frac{\theta_{\mathrm{c}}}{2}\right) K_{\mathrm{I}} - \frac{3}{2}\cos\left(\frac{\theta_{\mathrm{c}}}{2}\right)\sin(\theta_{\mathrm{c}})\, K_{\mathrm{II}}. \tag{81}$$

The crack propagates when the dynamic maximum hoop stress intensity factor K^* reached the dynamic crack initiation toughness K_{IC}, which is a material property and can be obtained from experiments. During the crack propagation, the crack speed is determined by making the maximum hoop stress intensity factor K^* equals the dynamic crack growth toughness K_{ID}. The relationship between the dynamic crack initiation toughness and the dynamic crack growth toughness is [51,52]

$$K_{\mathrm{ID}}(\dot{a}) = \frac{K_{\mathrm{IC}}}{1 - \left(\frac{C}{C_{\mathrm{R}}}\right)} \tag{82}$$

where C_{R} is the velocity of the Rayleigh waves. Thus the crack velocity C can be obtained from Eq. (82) as

$$C = \begin{cases} 0 & \text{if } K^* < K_{\mathrm{IC}} \\ C_{\mathrm{R}}\left(1 - \dfrac{K_{\mathrm{IC}}}{K^*}\right) & \text{otherwise.} \end{cases} \tag{83}$$

So a crack increment is defined by $\triangle l = C\triangle t$, where $\triangle t$ is the time step in the explicit algorithm.

5. Numerical examples and discussion

The proposed EMPM/EGIMP has been implemented in our MPM3D code [17,28], and several numerical examples are studied in this section to validate the method.

5.1. Opening crack in double cantilever beam

A double cantilever beam specimen (DCB) with a crack half way through the specimen at the mid-plane was end-loaded as shown in Fig. 4, which is the same as that calculated by Nairn [33]. This problem is studied in order to test the ability of the EMPM/EGIMP in modelling the crack. The material has a density of $\rho = 1.5$ g/cm^3, Young modulus of $E = 0.1$ MPa and Poisson ratio of $\nu = 0.33$. The end load is 0.4 mN and the specimen is $100 \times 24 \times 1$ (in mm). A uniform grid with a cell size of 5 mm $\times$ 3 mm is used (20×8 background meshes in the initial configuration). Two particles are placed in each direction in all cells for all the tests in this paper.

As shown in Fig. 5, the crack opens along the discontinuous line defined in advance, which shows that the EMPM has the ability of modelling discontinuity. The colour in Fig. 5 denotes the distribution of σ_{xx} while the simulation is damped to the static solution. The stress field describes reasonable behaviour with tensile bending stress on the crack surface, compression stress on the top and bottom surface and concentrating stress around the crack tip.

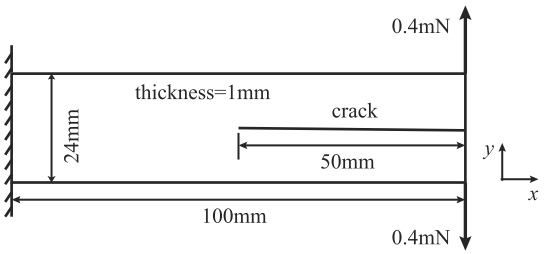

Fig. 4. A double cantilever beam specimen with a horizontal line crack at the mid-plane.

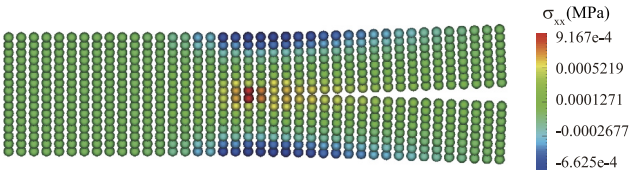

Fig. 5. Stress nephogram obtained by the EMPM. σ_{xx} scaled from blue (lowest) to red (highest). (For interpretation of the references to colour in this figure legend, the reader is referred to the web version of this article.)

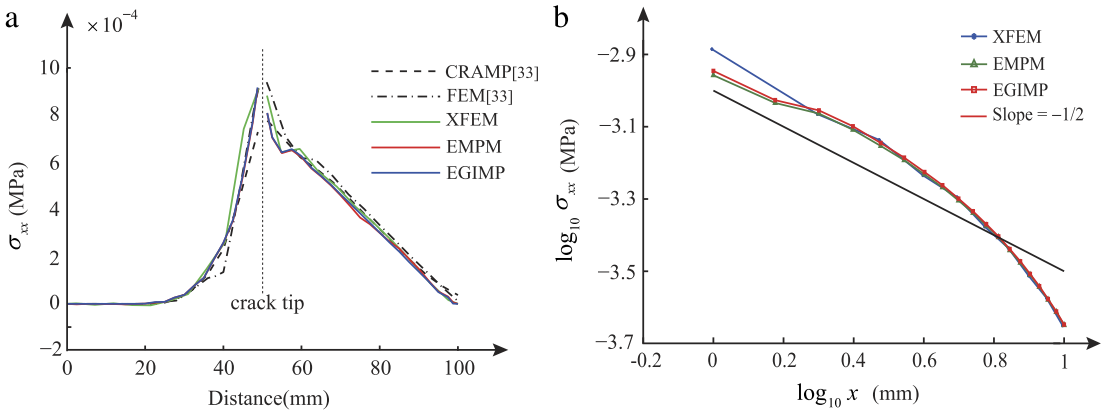

Fig. 6. Comparison of σ_{xx}. (a) σ_{xx} along the crack line. (b) Logarithmic graph near the crack tip. (For interpretation of the references to colour in this figure legend, the reader is referred to the web version of this article.)

To further test the performance of the EMPM/EGIMP, the σ_{xx} stress component along the crack line obtained by the EMPM, EGIMP, CRAMP [33], FEM [33] and XFEM with ABAQUS is compared in Fig. 6a. In the XFEM analysis, 21 $\times$ 9 elements are used to avoid putting the crack exactly on the element boundary. The particle stresses are extrapolated by the standard shape function to find the stress at the mid-plane (except the crack tip where has the $r^{-1/2}$ singularity). Fig. 6a shows that the results obtained by the EMPM and EGIMP agree well with those obtained by the other methods, and there is no remarkable difference between EMPM and EGIMP results in this small deformation problem.

We plot the logarithmic graph as shown in Fig. 6b to study the $r^{-1/2}$ singularity near the crack tip based on the theory of linear–elastic fracture mechanics. To get more information near the crack tip, we refine the meshes, where EMPM/EGIMP has 100 $\times$ 24 background meshes in the initial configuration and XFEM uses 101 $\times$ 25 element meshes. We compare the results at the positions where the distance is less than 10 mm from the crack tip in the mid-plane. Fig. 6b shows that the slope is close to $-1/2$ when $\log_{10}x < 0.4$ and then the slope changes for all the methods, which is reasonable.

The most time consuming part of the EMPM/EGIMP is the calculation of the nodal level set values in each time step. The comparison of CPU time between MPM and EMPM, GIMP and EGIMP is studied by this example with

Table 1
CPU time of MPM, EMPM and EGIMP.

	MPM	EMPM	GIMP	EGIMP
Time (s)	8.696	9.819	20.363	22.571

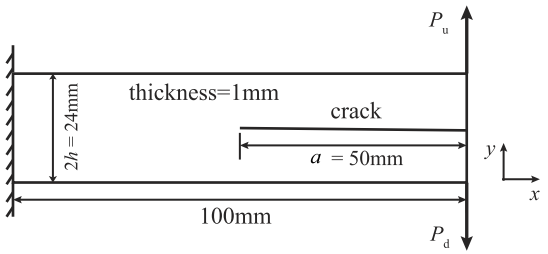

Fig. 7. Specimen with a horizontal line crack at the mid-plane used to compare the static stress intensity factors. The loads are applied at $t = 0$ and keep constants, those magnitude is 0.0004 N.

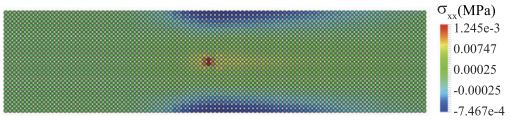

(a) Stress nephogram for pure mode I.

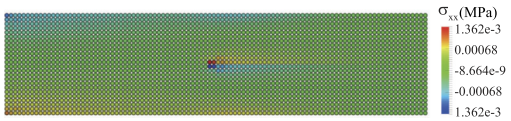

(b) Stress nephogram for pure mode II.

Fig. 8. Stress distributions for two types of crack mode obtained by the EMPM. σ_{xx} scales from blue (lowest) to red (highest). (For interpretation of the references to colour in this figure legend, the reader is referred to the web version of this article.)

size of 2.5 mm × 1.5 mm for 1000 ms. Table 1 listed the CPU time used by different methods, which shows that the EMPM/EGIMP with crack calculations will be approximately 10% slower than the MPM/GIMP.

In this simulation, the EMPM/EGIMP shows its ability of modelling cracks and gives accurate results as we expected. In the following sections, we will simulate different crack problems and calculate fracture parameters in the EMPM/EGIMP framework.

5.2. Static stress intensity factor

In this section, we calculate the stress intensity factors, K_{I} and K_{II}, by the method introduced in Section 4 under the assumption of plane stress, two-dimensional linear elasticity and static conditions. Consider the edge crack specimens shown in Fig. 7 (the same geometry with that in Section 5.1), which is the same as that studied by Guo and Nairn [42]. The plate has a width of 100 mm, height of 24 mm and thickness of 1 mm with a 50 mm edge crack. It is fixed at the left end and subjected to loads P_{u} and P_{d} at the top and bottom of the right end. $P_{\mathrm{u}} = -P_{\mathrm{d}}$ corresponds to the pure mode I crack load (double cantilever beam, DCB), while $P_{\mathrm{u}} = P_{\mathrm{d}}$ corresponds to the pure mode II crack load (end-notched flexure, ENF). The material has a density of $\rho = 1.5\ \mathrm{g/cm^3}$, Young modulus of $E = 2300$ MPa and Poisson ratio of $\nu = 0.33$. The simulation is damped to the static solution for comparison with the analytical solution. Three cases are simulated for each problem by employing different grid sizes (4 × 4 mm, 2 × 2 mm and 1 × 1 mm) to test convergence. There are 4 particles per cell all the time.

Fig. 8 illustrates the stress distributions obtained by the EMPM for two types of crack mode respectively. For the pure mode I, there are tensile bending stress on the crack surface, compression stress on the top and bottom surface and concentrating stress around the crack tip. However, for the pure mode II, there are bending stress on the bottom surface, compression stress on the top surface and both bending and compression stress around the crack tip.

For the DCB problem, the analytical solution of stress intensity factors is given by [53]

$$K_{\mathrm{Ia}} = 2\sqrt{3}\frac{P\,(a + \chi h)}{bh^{3/2}} \tag{84}$$

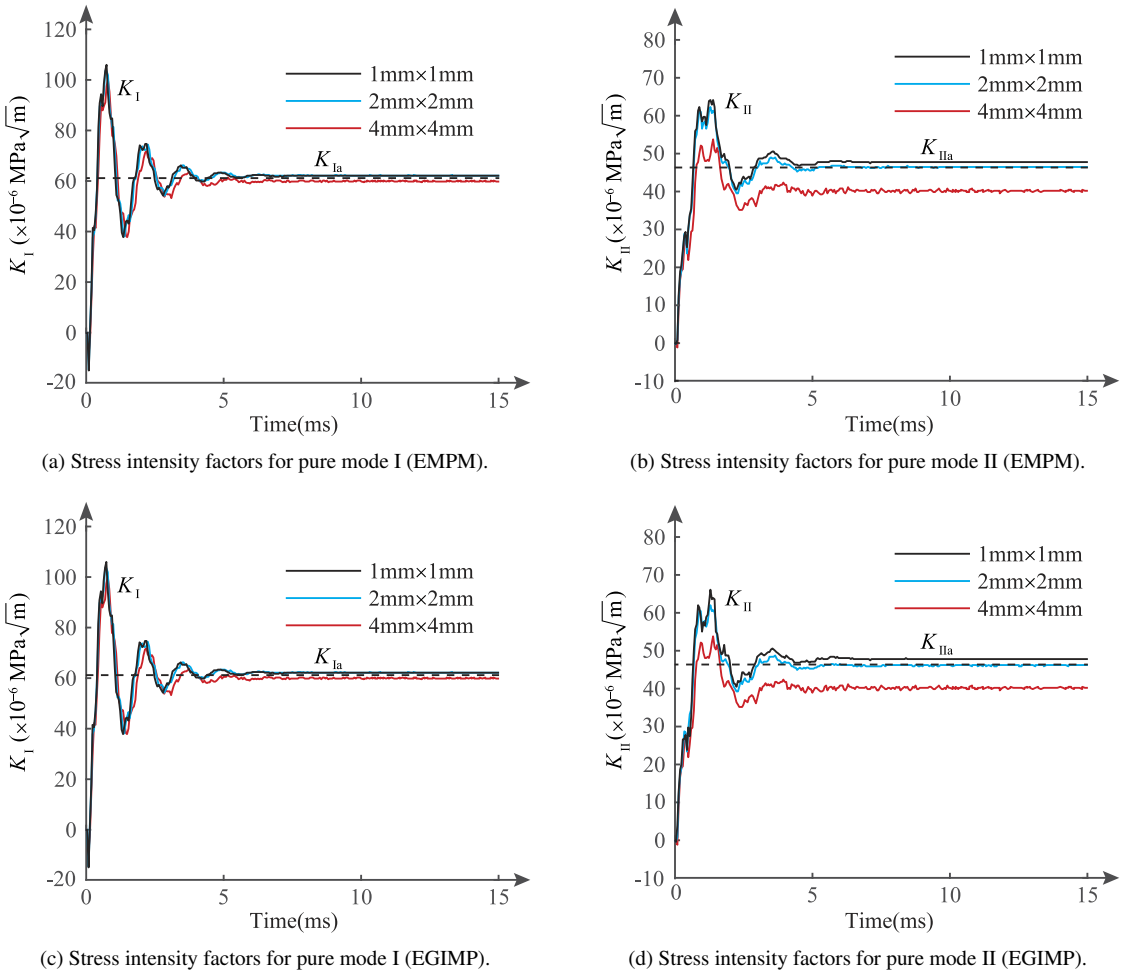

(a) Stress intensity factors for pure mode I (EMPM).

(b) Stress intensity factors for pure mode II (EMPM).

(c) Stress intensity factors for pure mode I (EGIMP).

(d) Stress intensity factors for pure mode II (EGIMP).

Fig. 9. Comparison of the stress intensity factors obtained by the EMPM and EGIMP with different mesh sizes from 1 mm × 1 mm up to 4 mm × 4 mm. (For interpretation of the references to colour in this figure legend, the reader is referred to the web version of this article.)

$$K_{IIa} = 0 \tag{85}$$

where a is the length of the crack, h is the half height of the specimen and $\chi = 2/3$ for isotropic material.

For the ENF problem, the analytical solution of stress intensity factors is given by [54]

$$K_{Ia} = 0 \tag{86}$$

$$K_{IIa} = \frac{3\ \mathrm{Pa}}{bh^{3/2}}\sqrt{1 + \frac{2\,(1+\nu)}{5}\left(\frac{h}{a}\right)^2} \tag{87}$$

where ν is Poisson ratio.

The time history of the stress intensity factors obtained by the EMPM/EGIMP for both DCB and ENF problems is shown in Fig. 9. At the beginning, the SIF increases from 0 with the reach of the stress wave. Then the values oscillate and tend to constant due to the damping. The static solutions agree well with the analytical solutions. For the DCB problem, even the coarsest mesh gives acceptable result. There is also no remarkable difference between EMPM and EGIMP results in this small deformation problem.

Furthermore, we simulate the mixed mode crack based on the means of the principle of superposition, which leads to $P_u = 0.0008$ N and $P_d = 0$ N. The EMPM and EGIMP both use a grid size of 2 × 2 mm. The time history of the

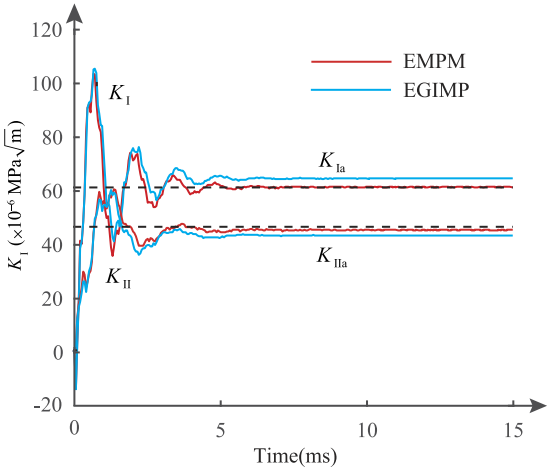

Fig. 10. The stress intensity factors for mixed mode crack.

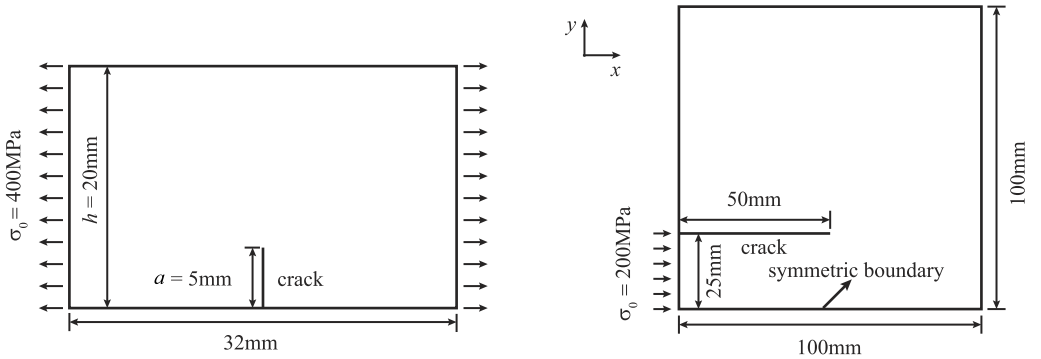

(a) A single edge notched tension plate specimen.

(b) Half of a double edge notched plate specimen.

Fig. 11. Specimen for dynamic stress intensity factors calculations. The loads are applied at $t = 0$ and keep constants.

stress intensity factors obtained by the EMPM and EGIMP is shown in Fig. 10. The EMPM/EGIMP result satisfies the superposition principle as expected.

5.3. Dynamic stress intensity factor

The calculation of fracture parameters under dynamic conditions is studied. Two specimens, a single edge notched tension (SENT) and a double edge notched plate (DENP) as shown in Fig. 11, are analysed under plane strain conditions.

For the SENT problem, the crack is pure mode I and the value of the applied stress is set to $\sigma_0 = 400$ MPa. The material has a density of $\rho = 5.0$ g/cm^3, Young modulus of $E = 200$ GPa and Poisson ratio of $\nu = 0.3$. The cell size is 0.5 mm and the particle space is 0.25 mm. The static, infinite-sheet stress intensity factor is given by

$$K_{I0} = \sigma_0 \sqrt{\pi a}. \tag{88}$$

Fig. 12a compares the time history of dynamic stress intensity factors, K_I, obtained by the EMPM/EGIMP with those obtained by the CRAMP and the finite difference method [1]. The stress intensity factors are normalized by K_{I0} obtained by Eq. (88). It is shown that the EMPM/EGIMP results agree well with other numerical results.

For the DENP problem, the crack is mixed mode and the value of the applied stress is set to $\sigma_0 = 200$ MPa. The specimen is not hold in a special loading fixture, but is completely free. Only the upper half of the specimen

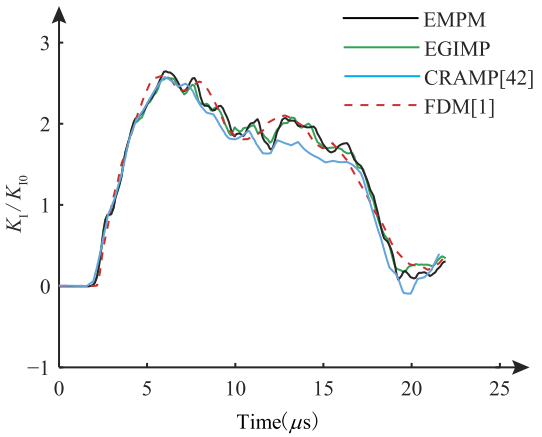

(a) Time history of mode I stress intensity factor for the SENT specimen obtained by the EMPM, EGIMP, CRAMP and FDM.

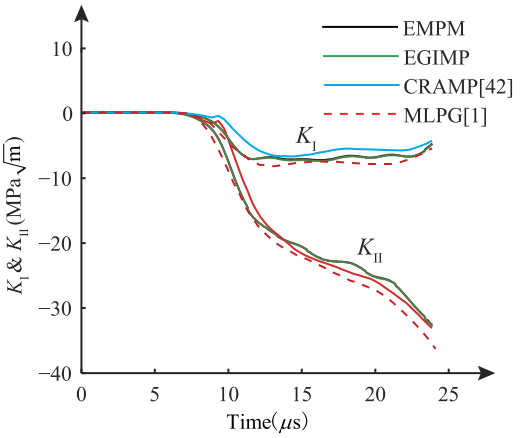

(b) Time history of mode I and mode II stress intensity factors for the DENP specimen obtained by the EMPM, EGIMP, CRAMP and MLPG.

Fig. 12. Comparison of stress intensity factors obtained by different numerical methods.

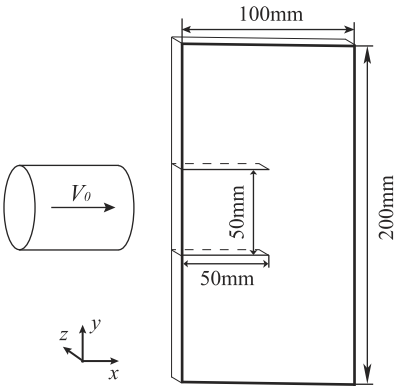

Fig. 13. Geometry of the Kalthoff's experiment.

is modelled due to symmetry. The nodal velocities in the y direction in the symmetry plane are set to zero. The material has a density of $\rho = 7.833$ g/cm^3, Young modulus of $E = 210$ GPa and Poisson ratio of $\nu = 0.29$. The cell size is 0.5 mm and the particle space is 0.25 mm. Fig. 12b compares the dynamic stress intensity factors, K_{I} and K_{II}, calculated by the EMPM/EGIMP with those calculated by the CRAMP and the Meshless Local Petrov–Galerkin (MLPG) method [16]. It is shown that the EMPM/EGIMP results agree well with other numerical results.

5.4. *Kalthoff's experiment*

In this section we numerically study the Kalthoff's experiment [55,56], which has been widely used for benchmarking the accuracy of crack propagation path. A plate with two initial edge notches is impacted by a projectile at speed V_0 as shown in Fig. 13. The experiment showed two different failure modes under low and high strain rates. In this paper, we focus on the low strain rate by choosing $V_0 = 20$ m/s, where the crack propagates with a global angle from 60° to 70°.

The material has a density of $\rho = 8000$ kg/m^3, Young modulus of $E = 190$ GPa and Poisson ratio of $\nu = 0.3$. The critical stress intensity factor is set to be $K_{Ic} = 68$ MPa$\sqrt{\mathrm{m}}$. Only half of the plate is simulated under the assumption of plane strain.

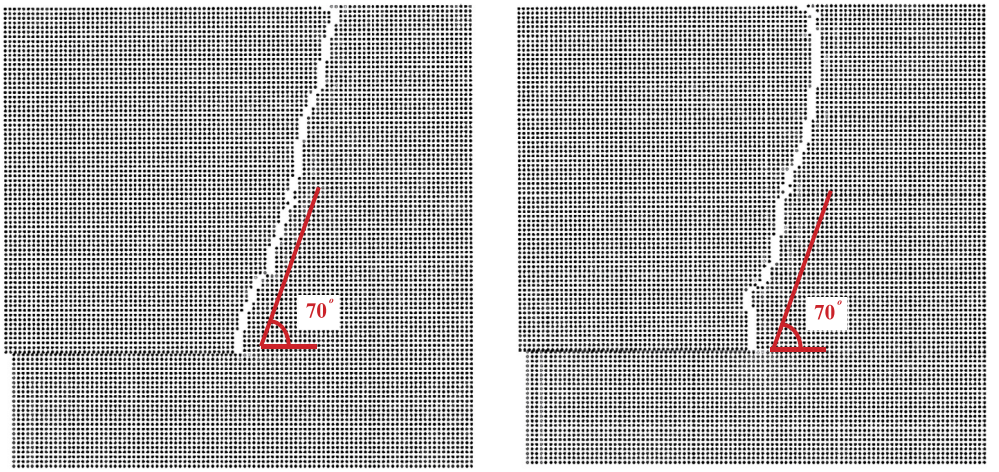

Fig. 14. Crack propagation path of the Kalthoff test for EMPM (left) and EGIMP (right).

Fig. 14 compares the crack propagation paths obtained by the EMPM/EGIMP. It can be seen that the path angle is close to 70° but the paths are not smooth. It is mainly because we cannot determine the exact crack tip direction in the present EMPM/EGIMP framework. The issue can be alleviated while introducing the crack tip enrichment or the cohesion model in the EMPM/EGIMP.

5.5. *Effect of integral path size on stress intensity factor*

The accuracy of stress intensity factors lies on the accuracy of J-integral, which is calculated by Eq. (67). In this paper, a square path close to the crack tip is chosen in the EMPM framework. Therefore, the effect of integral path size needs to be analysed.

For static problems, the area integral vanishes and the integral result is path independent theoretically. We repeated the DCB problem described in Section 5.2 for four different path sizes (from 3×3 cells up to 9×9 cells) and the cell size is 2 mm. The later path is very close to the boundary of the specimen. Fig. 15a plots the time history of stress intensity factors for the four different path sizes. As expected, the stress intensity factors are almost identical, which also shows that the other physical quantities such as stress field are correct. Therefore, it can be concluded that the effect of integral path size on stress intensity factor is neglectable. For the computational efficiency, the cells number of each side should not be too large, which increases the integral point number significantly. However, the path size relative to the crack should not be too small because of the high stress gradient, otherwise it reduces the computational accuracy.

For dynamic problem, the path independence property is lost. We repeated the DENP problem described in Section 5.3 for five different path sizes (from 3×3 cells up to 19×19 cells) and the other parameters remain the same. Fig. 15b plots the time history of stress intensity factors for the five different path sizes. In the early stages, the difference can be neglected for 3×3 cells up to 9×9 cells, while 19×19 cells has relatively obvious differences which is caused by the stress wave transmission. With the wave reflection, the differences become apparent for all the results but in an acceptable range. As the conclusion in CRAMP [42], the recommendation is that the EMPM/EGIMP calculations of J integral should use a small path.

5.6. *Effect of mesh size on stress intensity factor*

In this section we study the effect of the background mesh size. The calculation time mainly depends on the cell size. For a two dimensional problem, each factor of 0.5 in cell size leads to a factor of 8 increase in calculation time. Therefore, a relatively coarse mesh can reduce enormous calculation time. As in the CRAMP, the EMPM/EGIMP computes the stress intensity factors by J-integral, which gives the good results even for a relatively coarse mesh.

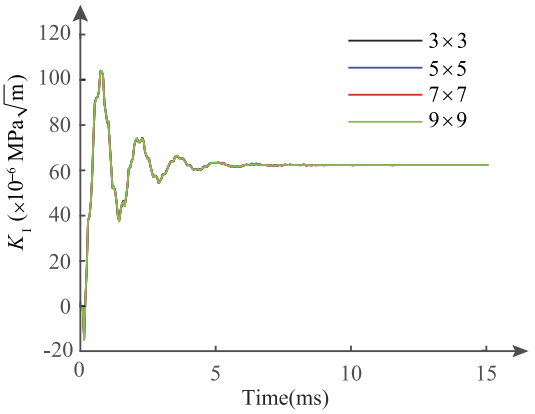

(a) Time history of static stress intensity factors.

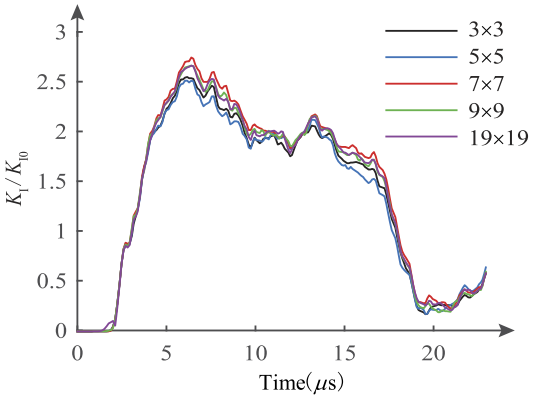

(b) Time history of dynamic stress intensity factors.

Fig. 15. Effect of integral path size on stress intensity factor.

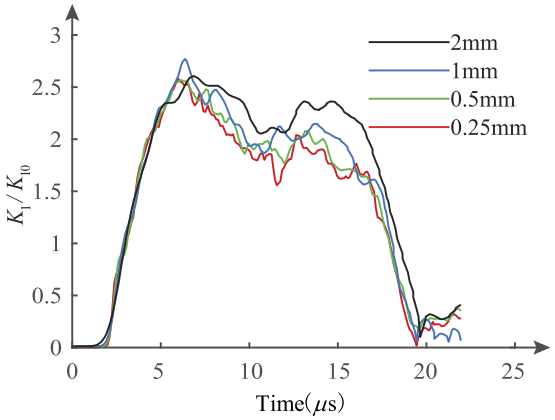

Fig. 16. Time history of dynamic stress intensity factors for different grid sizes.

However, the direct method, which calculates the stress intensity factors from crack-tip stress field and displacement field, requires the finer mesh.

We repeat the DENP problem described in Section 5.3 for four different grid sizes (from 0.25 mm up to 2 mm) and the crack has the length of 5 mm. Fig. 16 plots the time history of normalized dynamic stress intensity factors for the four cases. The 0.5 mm grid gives very close results to the 0.25 mm grid, while the 1 mm grid gives quite close results to the 0.25 mm grid. Although the cell size of the coarsest grid (2 mm grid) is 8 times of the finest grid (0.25 mm grid), it still gives reasonable results, which shows that the EMPM possesses good convergence in space. The computational cost of the 1 mm grid is only 1/64 of the 0.25 mm grid in 2D problem.

6. Conclusion

In this paper, the EMPM/EGIMP is developed for modelling crack problems by introducing the idea of the XFEM into the MPM/GIMP framework. The EMPM/EGIMP enriches the nodal degrees of freedom in the region around the crack and jump function is chosen as the enrichment function to describe the crack. The discretization scheme of the EMPM/EGIMP is derived based on the weak form of the momentum conservation equations, just as the conventional MPM/GIMP. The technique we lump the mass matrix makes the EMPM/EGIMP can be implemented easily in a conventional MPM/GIMP code and can degenerate to the conventional MPM/GIMP when there is no crack. The level set method is also introduced in the EMPM/EGIMP, which can give the exact location of crack surface. The level set

function values are carried by particles and are mapped to the grid nodes in each time step in the same way as other physical quantities. Therefore, it requires a small additional computational cost than the conventional MPM/GIMP. Comparison between MPM/GIMP and EMPM/EGIMP shows the crack calculations to be approximately 10% slower. The increased time includes two parts, calculating the level sets for the particles at the beginning and updating the level sets for the nodes at each timestep.

Numerical examples show that the EMPM/EGIMP is accurate to the level of ABAQUS XFEM and CRAMP for the symmetric horizontal crack problem. For both the static and dynamic problems, the fracture parameters also agree well with the analytical solution and other numerical methods, which illustrate the good performance of the EMPM/EGIMP. Based on the LSM tracking crack surface and accurate calculation of fracture parameters, crack propagation is implemented in the EMPM/EGIMP framework, which gives the similar crack path with the Kalthoff's experiment. The LSM values of particles around the crack tip should be recalculated as the crack propagates, which does not bring additional computational cost except in the region of the crack tip. For the small deformation problems in this paper, there is no remarkable difference between EMPM and EGIMP results.

References

[1] Y. Chen, M. Wilkins, Numerical analysis of dynamic crack problems, Mech. Fract. 4 (1977) 295–345.
[2] C. Miehe, E. Gürses, A robust algorithm for configurational-force-driven brittle crack propagation with R-adaptive mesh alignment, Internat. J. Numer. Methods Engrg. 72 (2) (2007) 127–155.
[3] X.-P. Xu, A. Needleman, Numerical simulations of fast crack growth in brittle solids, J. Mech. Phys. Solids 42 (9) (1994) 1397–1434.
[4] T. Belytschko, J. Fish, B.E. Engelmann, A finite element with embedded localization zones, Comput. Methods Appl. Mech. Engrg. 70 (1) (1988) 59–89.
[5] N. Moes, J. Dolbow, T. Belytschko, A finite element method for crack growth without remeshing, Internat. J. Numer. Methods Engrg. 46 (1) (1999) 131–150.
[6] N. Sukumar, T. Belytschko, Arbitrary branched and intersecting cracks with the extended finite element method, Internat. J. Numer. Methods Engrg. 48 (2000) 1741–1760.
[7] E. Budyn, G. Zi, N. Moës, T. Belytschko, A method for multiple crack growth in brittle materials without remeshing, Internat. J. Numer. Methods Engrg. 61 (10) (2004) 1741–1770.
[8] N. Sukumar, N. Moës, B. Moran, T. Belytschko, Extended finite element method for three-dimensional crack modelling, Internat. J. Numer. Methods Engrg. 48 (11) (2000) 1549–1570.
[9] Q. Zeng, Z. Liu, D. Xu, Z. Zhuang, Modeling stationary and moving cracks in shells by X-FEM with CB shell elements, Sci. China Technol. Sci. 57 (7) (2014) 1276–1284.
[10] J. Zhao, Y. Li, W.K. Liu, Predicting band structure of 3D mechanical metamaterials with complex geometry via XFEM, Comput. Mech. 55 (4) (2015) 659–672.
[11] B. Lecampion, An extended finite element method for hydraulic fracture problems, Int. J. Numer. Methods Biomed. Eng. 25 (2) (2009) 121–133.
[12] T. Mohammadnejad, A. Khoei, An extended finite element method for hydraulic fracture propagation in deformable porous media with the cohesive crack model, Finite Elem. Anal. Des. 73 (2013) 77–95.
[13] T. Belytschko, Y. Krongauz, D. Organ, M. Fleming, P. Krysl, Meshless methods: an overview and recent developments, Comput. Methods Appl. Mech. Engrg. 139 (1) (1996) 3–47.
[14] D. Organ, M. Fleming, T. Terry, T. Belytschko, Continuous meshless approximations for nonconvex bodies by diffraction and transparency, Comput. Mech. 18 (3) (1996) 225–235.
[15] T. Belytschko, L. Gu, Y. Lu, Fracture and crack growth by element free Galerkin methods, Modelling Simulation Mater. Sci. Eng. 2 (3A) (1994) 519.
[16] R. Batra, H. Ching, Analysis of elastodynamic deformations near a crack/notch tip by the meshless local Petrov-Galerkin (MLPG) method, CMES Comput. Model. Eng. Sci. 3 (6) (2002) 717–730.
[17] X. Zhang, Z. Chen, Y. Liu, The Material Point Method: A Continuum-Based Particle Method for Extreme Loading Cases, Academic Press, 2016.
[18] D. Sulsky, Z. Chen, H.L. Schreyer, A particle method for history-dependent materials, Comput. Methods Appl. Mech. Engrg. 118 (1994) 179–186.
[19] S.G. Bardenhagen, E.M. Kober, The generalized interpolation material point method, CMES Comput. Model. Eng. Sci. 5 (6) (2004) 477–495.
[20] W. Gong, Y. Liu, X. Zhang, H. Ma, Numerical investigation on dynamical response of aluminum foam subject to hypervelocity impact with material point method, CMES Comput. Model. Eng. Sci. 83 (5) (2012) 527–545.
[21] Y. Liu, H.-K. Wang, X. Zhang, A multiscale framework for high-velocity impact process with combined material point method and molecular dynamics, Int. J. Mech. Mater. Des. 9 (2) (2013) 127–139.
[22] S. Ma, X. Zhang, X. Qiu, Comparison study of MPM and SPH in modeling hypervelocity impact problems, Int. J. Impact Eng. 36 (2) (2009) 272–282.
[23] P. Huang, X. Zhang, S. Ma, H. Wang, Shared memory OpenMP parallelization of explicit MPM and its application to hypervelocity impact, CMES Comput. Model. Eng. Sci. 38 (2) (2008) 119–148.

[24] W. Hu, Z. Chen, Model-based simulation of the synergistic effects of blast and fragmentation on a concrete wall using the MPM, Int. J. Impact Eng. 32 (12) (2006) 2066–2096.
[25] S. Ma, X. Zhang, Y. Lian, X. Zhou, Simulation of high explosive explosion using adaptive material point method, CMES Comput. Model. Eng. Sci. 39 (2) (2009) 101.
[26] Y. Wang, H. Beom, M. Sun, S. Lin, Numerical simulation of explosive welding using the material point method, Int. J. Impact Eng. 38 (1) (2011) 51–60.
[27] D. Sulsky, S.-J. Zhou, H.L. Schreyer, Application of a particle-in-cell method to solid mechanics, Comput. Phys. Comm. 87 (1) (1995) 236–252.
[28] Z. Ma, X. Zhang, P. Huang, An object-oriented MPM framework for simulation of large deformation and contact of numerous grains, CMES Comput. Model. Eng. Sci. 55 (1) (2010) 61.
[29] W. Gong, X. Zhang, X. Qiu, Numerical study of dynamic compression process of aluminum foam with material point method, CMES Comput. Model. Eng. Sci. 82 (3-4) (2011) 195–213.
[30] P. Yang, Y. Liu, X. Zhang, X. Zhou, Y. Zhao, Simulation of fragmentation with material point method based on Gurson model and random failure, CMES Comput. Model. Eng. Sci. 85 (3) (2012) 207–237.
[31] L.M. Shen, A rate-dependent damage/decohesion model for simulating glass fragmentation under impact using the material point method, CMES Comput. Model. Eng. Sci. 49 (1) (2009) 23–45.
[32] D.Z. Zhang, Q. Zou, W.B. VanderHeyden, X. Ma, Material point method applied to multiphase flows, J. Comput. Phys. 227 (6) (2008) 3159–3173.
[33] J.A. Nairn, Material point method calculations with explicit cracks, CMES Comput. Model. Eng. Sci. 4 (6) (2003) 649–663.
[34] B. Wang, V. Karuppiah, H. Lu, R. Komanduri, S. Roy, Two-dimensional mixed mode crack simulation using the material point method, Mech. Adv. Mater. Struct. 12 (6) (2005) 471–484.
[35] N.P. Daphalapurkar, H. Lu, D. Coker, R. Komanduri, Simulation of dynamic crack growth using the generalized interpolation material point (GIMP) method, Int. J. Fract. 143 (1) (2007) 79–102.
[36] Z. Chen, R. Feng, X. Xin, L. Shen, A computational model for impact failure with shear-induced dilatancy, Internat. J. Numer. Methods Engrg. 56 (14) (2003) 1979–1997.
[37] P. Yang, Y. Gan, X. Zhang, Z. Chen, W. Qi, P. Liu, Improved decohesion modeling with the material point method for simulating crack evolution, Int. J. Fract. 186 (1–2) (2014) 177–184.
[38] P.C. Wallstedt, J. Guilkey, An evaluation of explicit time integration schemes for use with the generalized interpolation material point method, J. Comput. Phys. 227 (22) (2008) 9628–9642.
[39] T. Belytschko, M. Stolarska, D.L. Chopp, N. Moes, Modelling crack growth by level sets in the extended finite element method, Internat. J. Numer. Methods Engrg. 51 (2001) 943–960.
[40] G. Cherepanov, The propagation of cracks in a continuous medium, J. Appl. Math. Mech. 31 (3) (1967) 503–512.
[41] J.R. Rice, A path independent integral and the approximate analysis of strain concentration by notches and cracks, J. Appl. Mech. 35 (2) (1968) 379–386.
[42] Y.J. Guo, J.A. Nairn, Calculation of J-integral and stress intensity factors using the material point method, CMES Comput. Model. Eng. Sci. 6 (3) (2004) 295–308.
[43] J. Nairn, Y. Guo, Material point method calculations with explicit cracks, fracture parameters, and crack propagation, in: 11th International Conference on Fracture, Turin, Italy, 2005.
[44] G.P. Cherepanov, Mechanics of Brittle Fracture, McGraw-Hill Inc., 1979.
[45] T. Nishioka, Recent developments in computational dynamic fracture mechanics, in: Dynamic Fracture Mechanics, Computational Mechanics Publications, 1995.
[46] T. Nishioka, S. Atluri, A numerical study of the use of path independent integrals in elasto-dynamic crack propagation, Eng. Fract. Mech. 18 (1) (1983) 23–33.
[47] T. Nishioka, R. Murakami, Y. Takemoto, The use of the dynamic J integral (J') in finite-element simulation of mode I and mixed-mode dynamic crack propagation, Int. J. Press. Vessels Pip. 44 (3) (1990) 329–352.
[48] T. Nishioka, S. Atluri, Path-independent integrals, energy release rates, and general solutions of near-tip fields in mixed-mode dynamic fracture mechanics, Eng. Fract. Mech. 18 (1) (1983) 1–22.
[49] F. Erdogan, G. Sih, On the crack extension in plates under plane loading and transverse shear, J. Basic Eng. 85 (4) (1963) 519–527.
[50] L. Freund, Crack propagation in an elastic solid subjected to general loading –I. Constant rate of extension, J. Mech. Phys. Solids 20 (3) (1972) 129–140.
[51] D. Grégoire, H. Maigre, J. Rethore, A. Combescure, Dynamic crack propagation under mixed-mode loading –comparison between experiments and X-FEM simulations, Int. J. Solids Struct. 44 (20) (2007) 6517–6534.
[52] M.F. Kanninen, C.L. Popelar, Advanced Fracture Mechanics, Oxford University Press, 1985.
[53] M. Kanninen, An augmented double cantilever beam model for studying crack propagation and arrest, Int. J. Fract. 9 (1) (1973) 83–92.
[54] L. Carlsson, J. Gillespie, R. Pipes, On the analysis and design of the end notched flexure (ENF) specimen for mode II testing, J. Compos. Mater. 20 (6) (1986) 594–604.
[55] J.F. Kalthoff, Modes of dynamic shear failure in solids, Int. J. Fract. 101 (1–2) (2000) 1–31.
[56] J. Kalthoff, S. Winkler, Failure mode transition at high rates of shear loading. DGM Informationsgesellschaft mbH, Impact Loading Dynam. Behav. Mater. 1 (1988) 185–195.